

# Magnetic Dichroism in Rutile NiF<sub>2</sub>: Separating Altermagnetic and Ferromagnetic Effects

A. Hariki,<sup>1,\*</sup> K. Sakurai,<sup>1</sup> T. Okauchi,<sup>1</sup> and J. Kuneš<sup>2</sup>

<sup>1</sup>*Department of Physics and Electronics, Graduate School of Engineering, Osaka Metropolitan University, 1-1 Gakuen-cho, Nakaku, Sakai, Osaka 599-8531, Japan*

<sup>2</sup>*Department of Condensed Matter Physics, Faculty of Science, Masaryk University, Kotlářská 2, 611 37 Brno, Czechia*

We present numerical simulations of x-ray magnetic circular dichroism (XMCD) at the L<sub>2,3</sub> edge of Ni in the weakly ferromagnetic altermagnet NiF<sub>2</sub>. Our results predict a significant XMCD signal for light propagating perpendicular to the magnetic moments, which are approximately aligned along the [100] easy-axis direction. The analysis shows that the altermagnetic and ferromagnetic contributions to the XMCD signal can be uniquely distinguished by their dependence on an applied magnetic field. By varying the angle of the field relative to the easy axis, the in-plane orientation of both the Néel vector and the net magnetization can be systematically controlled. We further demonstrate that the XMCD signal, even under fields as strong as 40 T and for any in-plane orientation, can be accurately described as a linear combination of two spectral components, with geometrical prefactors determined by the field's magnitude and direction. This insight enables experimental validation of the distinctive relationship between the Néel vector orientation and the x-ray Hall vector in the rutile structure. Quantitative simulations supporting these findings are provided.

## I. INTRODUCTION

The identification of altermagnets [1, 2] marks the emergence of a new class of collinear magnets, which, despite having no net magnetization, enable the existence of spin-polarized bands [1–12], anomalous Hall effect [6, 10, 13–18], odd magneto-optical effects [15, 19–21], and various other phenomena [22] characterized by odd Néel vector dependence.

Distinguished from conventional collinear magnets such as ferromagnets and antiferromagnets by non-relativistic symmetry operations, the characterization of altermagnets is rooted in separation between electron

spin and its orbital motion. In real-world materials, however, relativistic effects such as spin-orbit coupling (SOC) invariably come into play. While typically considered a perturbation to non-relativistic symmetry, SOC becomes a critical factor for the observation of altermagnetic phenomena in some experiments [23]. Indeed, the influence of SOC is twofold: on one hand, it is indispensable for manifesting altermagnetic effects in optical and transport properties, enabling phenomena such as anomalous Hall currents or linear magneto-optical effects. On the other hand, the presence of SOC leads to competing effects, such as weak ferromagnetism, which can obscure or even mimic altermagnetic responses. This duality poses a key challenge in disentangling these intertwined behaviors experimentally. To address this challenge, x-ray spectroscopy has emerged as a powerful probe for isolating intrinsic altermagnetic effects from those induced or modified by SOC. While SOC is a prerequisite for observing magnetic dichroism, the x-ray magnetic circular dichroism (XMCD) technique leverages the large spin-orbit splitting inherent to core states, which is fundamentally distinct from weak ferromagnetism or other valence band effects. Computational studies indicate that the contribution of valence SOC to XMCD spectra is generally minor in many compounds containing 3d elements [20, 25].

In this Article we demonstrate this point in computational study of the XMCD on the Ni L<sub>2,3</sub> edge in NiF<sub>2</sub>. NiF<sub>2</sub>, like other members of the transition metal difluoride series, crystallizes in rutile structure and antiferromagnetically orders below 73.2 K [26]. Unlike other compounds in the series with the [001] easy axis, the Néel vector  $\mathbf{L} = \mathbf{m}_1 - \mathbf{m}_2$  points along [010] or the other three direction related by the tetragonal symmetry [27, 28]. This orientation allows finite XMCD for the light propagation vector  $\mathbf{k} = [100]$ . The valence SOC causes a small

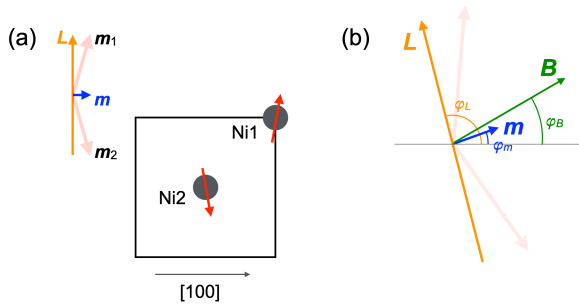


FIG. 1. (a) Top view of the rutile structure with the Néel vector  $\mathbf{L}$  in the [010] direction. The red arrows mark the local moments  $\mathbf{m}_{1,2}$  in the Ni sites,  $\mathbf{m}$  is the net magnetization. (b) The definitions of angles  $\varphi_B$ ,  $\varphi_L$  and  $\varphi_m$  where  $\mathbf{B}$  in the magnetic field applied in the (001) plane.

\* A.H. and K.S. contributed equally to this work.

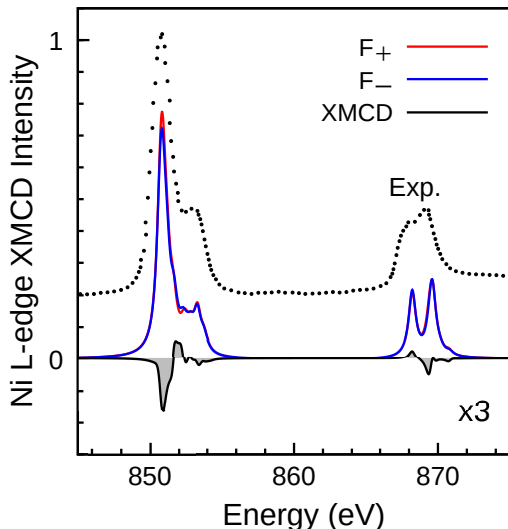


FIG. 2. The XAS calculated for the two circular polarizations (red and blue) at the Ni  $L_{2,3}$  edge together with the XMCD intensities (shaded). The calculated spectral intensities are broadened by a Lorentzian of 0.30 eV (HWHM). The experimental Ni  $L_{2,3}$ -edge XAS spectrum taken from Ref. 24 is shown for comparison. The experimental baseline was offset for the sake of clarity.

canting of the Ni moments, which results in a net spin polarization of about  $0.03 \mu_B$  in the  $[100]$  direction [28, 29] and gives rise to conventional ferromagnetic XMCD signal.

Applying magnetic field  $\mathbf{B}$  in the  $(001)$  plane one can vary the moments canting as well as the orientation of the Néel vector  $\mathbf{L}$ . We simulate such an experimental set-up and show that the frequency dependent Hall vector  $\mathbf{h}(\omega) = \text{Im}(\sigma_{zy}^a(\omega), \sigma_{xz}^a(\omega), \sigma_{yx}^a(\omega))$  can be to a high accuracy described by two spectral functions  $\Delta_{\text{ALT}}(\omega)$  and  $\Delta_{\text{FM}}(\omega)$

$$\mathbf{h}(\omega) = \Delta_{\text{ALT}}(\omega)\hat{\mathbf{L}}_{(110)} + \Delta_{\text{FM}}(\omega)\mathbf{m}(\mathbf{B}). \quad (1)$$

Here,  $\hat{\mathbf{L}}$  is the unit vector in the direction of  $\mathbf{L}$ ,  $\mathbf{m}$  is the net magnetic moment per atom and  $\mathcal{M}_{(110)}$  is the operation of mirror symmetry by the  $(110)$  plane. The XMCD spectra for light propagating in the  $\hat{\mathbf{k}}$  direction is obtained as  $F_{\text{XMCD}} = 2\mathbf{h}(\omega) \cdot \hat{\mathbf{k}}$ . Expressing the conductivity tensor in terms of several fundamental spectral functions follows the spirit of Refs. [25, 30–33] and leads to particularly simple form (1) in case of rutile structure.

## II. RESULTS

In Fig. 2, we demonstrate that our calculations accurately capture well the experimental x-ray absorption spectra (XAS) of  $\text{NiF}_2$ , which are dominated by atomic multiplet features. Note that we use a single value for the lifetime broadening, which somewhat exaggerates the sharpness of the  $L_2$  features.

The orientation and size of the Néel vector  $\mathbf{L}$  and magnetization  $\mathbf{m}$  vectors is determined by the external field  $\mathbf{B}$ , the inter-atomic exchange  $J_i$  and the single-ion anisotropy (SIA). We treat the inter-atomic exchange on the mean-field level while SIA appears through solution of the atomic problem with SOC and crystal-field. We begin our presentation with  $\mathbf{B} \parallel [100]$ . In this configuration, as reported in Ref. 35, a field of 0.7 T is sufficient to select the  $[100]$  domain (out of the four possible  $\mathbf{L}$  orientations). Increasing the magnetic field leads to a growth of  $|\mathbf{m}|$ . In Fig. 3(a) we present the XMCD spectra for  $\hat{\mathbf{k}}$  along the applied field. The Hall vector points along  $[100]$  direction and has an amplitude  $h(\omega) = \Delta_{\text{ALT}}(\omega) + \Delta_{\text{FM}}(\omega)|\mathbf{m}|$ . In the absence of an external field, the calculated net magnetization is  $|\mathbf{m}| = 0.03 \mu_B$  per atom, consistent with theoretical predictions [29] and experimental measurements [28]. The XMCD spectra calculated for various applied fields allow us to extract  $\Delta_{\text{ALT}}(\omega)$  and  $\Delta_{\text{FM}}(\omega)$ , as shown in Fig. 3(c). The validity of Eq. 1 is confirmed in Fig. 3(a,b). Fields up to 10 T result in more than a twofold increase of  $|\mathbf{m}|$ , providing sufficient variation of the XMCD spectra to facilitate a similar analysis of typical experimental data.

Next, we rotate the applied field,  $\mathbf{B} = B(\cos \varphi_B, \sin \varphi_B, 0)$ , in the  $(001)$  plane, as illustrated in Fig. 1(b). The calculated orientations of  $\mathbf{L}$  and  $\mathbf{m}$ , along with the magnitude  $|\mathbf{m}|$ , are shown in Fig. 4. These results align well with previous theoretical and experimental studies [28, 29]. The magnetic order arises from a competition between SIA, which favors the  $[010]$  and  $[100]$  orientations of  $\mathbf{L}$  and  $\mathbf{m}$ , respectively, and the external field, which  $\mathbf{L}$  and  $\mathbf{m}$  being perpendicular, with  $\mathbf{m} \parallel \mathbf{B}$ . At low field strengths, the orientations of the magnetic moments are only slightly perturbed. In the highest studied field of 40 T, the net magnetization  $\mathbf{m}$  follows the rotation of  $\mathbf{B}$ , though it remains misaligned, while the orthogonality of  $\mathbf{m}$  and  $\mathbf{L}$  is approximately maintained, reflecting the rigidity of Ni moments.

In Fig. 5 we show the field dependence of the XMCD spectra for the incoming light directions  $[100]$  and  $[010]$ . A key observation is the comparison of the full calculation, which accounts for specific orientations of the Ni moments, and the spectra derived using Eq. 1 with the previously obtained spectral distributions  $\Delta_{\text{ALT}}(\omega)$  and  $\Delta_{\text{FM}}(\omega)$ . We find that for all studied field strengths, up to 40 T, and across all field angles  $\varphi_B$ , Eq. 1 describes the calculated spectra with a relative accuracy better than 1%.

Finally, we present the data in a form that is closely aligned with a potential experimental setup. In this configuration, the external field  $\mathbf{B}$  is parallel to the light beam  $\hat{\mathbf{k}}$ , and the sample is rotated along the  $c$ -axis, which is perpendicular to the beam. For  $B = 0$  the Néel and magnetization vectors rotate with the sample, resulting in a  $\cos \varphi_B$  dependence of the spectra. For a finite field

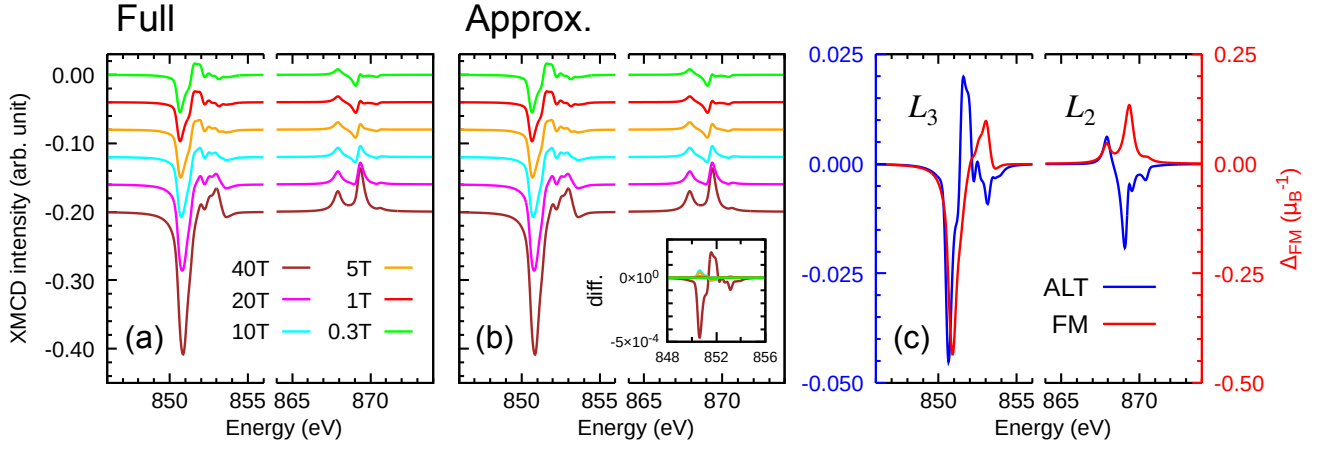


FIG. 3. (a) Ni  $L_{2,3}$ -edge XMCD intensities in  $\text{NiF}_2$  calculated for various amplitudes of the magnetic field  $B$  with  $\varphi_B = 0^\circ$ . (b) XMCD intensities computed as a linear combination of (c)  $\Delta_{\text{ALT}}(\omega)$  (blue, left axis) and  $\Delta_{\text{FM}}(\omega)$  (red, right axis). The inset in panel (b) shows the difference in the XMCD intensities at the Ni  $L_3$ -edge between the full calculations in (a) and the approximations in (b).

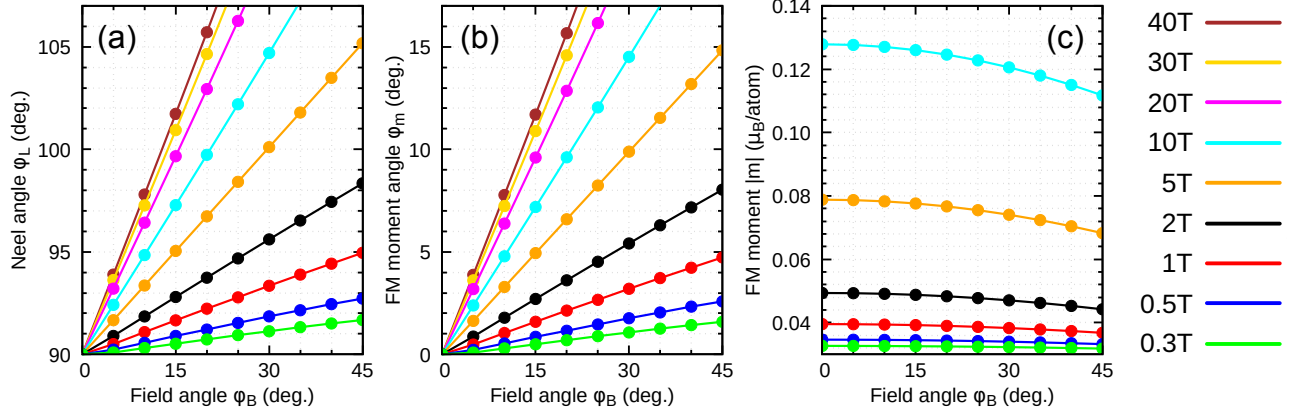


FIG. 4. Relation between the angles of the external field  $\varphi_B$  and (a) the Néel vector  $\varphi_L$ , (b) the FM moment  $\varphi_m$ , and (c) the amplitude of the FM moment  $|\mathbf{m}(\mathbf{B})|$  for selected amplitudes of the external field  $\mathbf{B}$ . The results over a wider range for the angles and amplitudes are provided in Fig. S4 of the Supplementary Material [34].

the XMCD spectrum is described by Eq. 1 as

$$\begin{aligned}
 F_{\text{XMCD}}(\omega) &= \\
 &\Delta_{\text{ALT}}(\omega) \sin(\varphi_L + \varphi_B) + \Delta_{\text{FM}}(\omega) |\mathbf{m}| \cos(\varphi_m - \varphi_B) \\
 &\approx \Delta_{\text{ALT}}(\omega) \cos(1 + \alpha) \varphi_B + \Delta_{\text{FM}}(\omega) m_0 \cos(1 - \alpha) \varphi_B,
 \end{aligned} \tag{2}$$

where  $\varphi_L$ ,  $\varphi_m$  and  $|\mathbf{m}|$  depend on  $\varphi_B$  and the field amplitude, as illustrated in Fig. 4. Using the leading-order approximation  $\varphi_L \simeq \varphi_m + \pi/2$ ,  $|\mathbf{m}| \simeq m_0$  and  $\varphi_m \simeq \alpha \varphi_B$ , where  $\alpha$  and  $m_0$  depend on the field amplitude, we arrive at the bottom line. For sufficiently large fields ( $\alpha \approx 0.57$  at 10 T) this dependence allows for experimental verification of the relationship  $\hat{\mathbf{h}}_{\text{ALT}} = \mathcal{M}_{(110)} \hat{\mathbf{L}}(\mathbf{B})$  between the in-plane orientation of the Néel vector  $\mathbf{L}$  and the direction of the altermagnetic part of the Hall vector  $\hat{\mathbf{h}}_{\text{ALT}}$

in the x-ray range. The results of a simulation for a field of 10 T are shown in Fig. 6.

### III. DISCUSSION

We have conducted numerical simulations of XMCD at the  $L_{2,3}$  edge of Ni in the rutile altermagnet  $\text{NiF}_2$  under an external magnetic field. Our results demonstrate that the XMCD signal across a wide range of field amplitudes and  $ab$ -plane orientations can be expressed as a linear combination of two distinct spectral functions. These functions represent the altermagnetic and ferromagnetic contributions. The coefficients of this linear combination depend on the orientations of the Néel  $\mathbf{L}$  and the magnetization  $\mathbf{m}$  vectors. The ferromagnetic

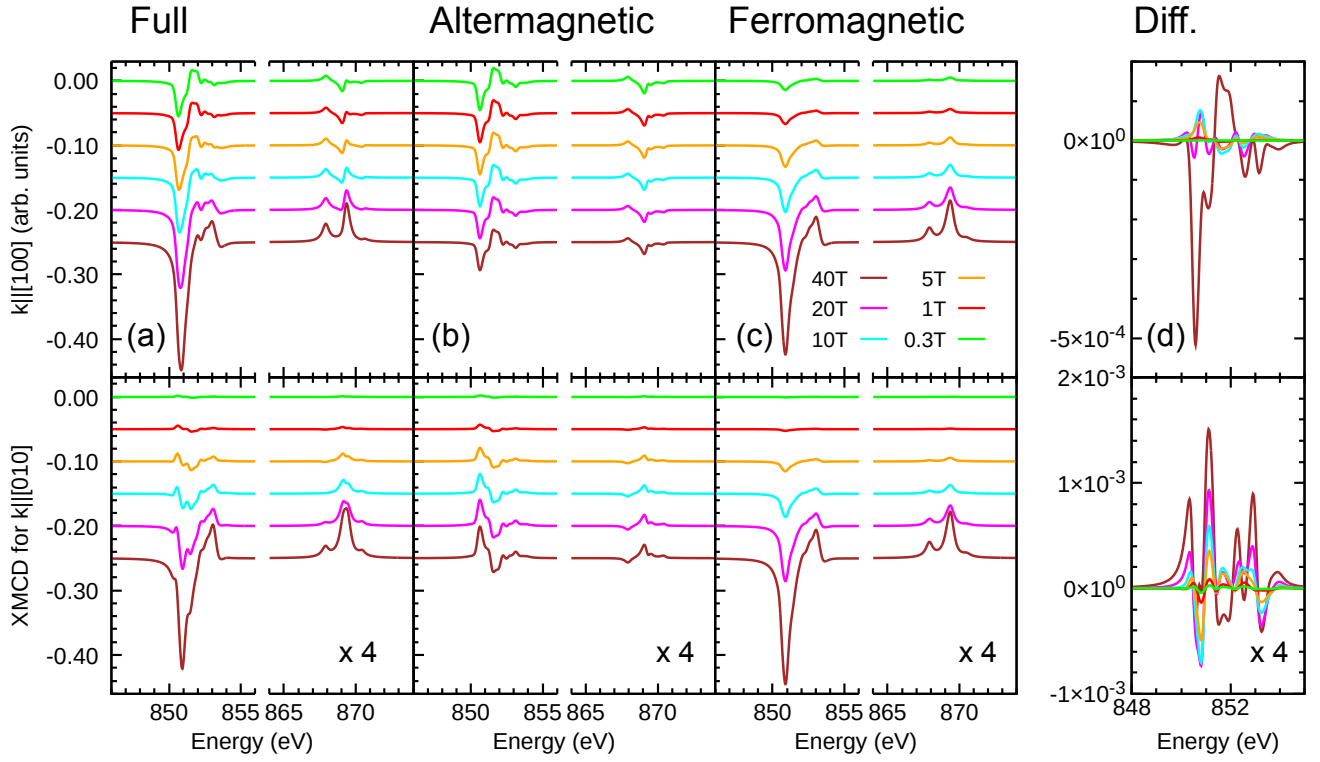


FIG. 5. (a) Ni  $L_{2,3}$ -edge XMCD intensities in  $\text{NiF}_2$  calculated for various amplitudes of the magnetic field  $B$  with  $\varphi_B = 20^\circ$  for the two geometries of the light propagation vector  $\hat{\mathbf{k}} = [100]$  (top) and  $\hat{\mathbf{k}} = [010]$  (bottom). (b) The altermagnetic contributions and (c) the ferromagnetic contributions. (d) The difference in the XMCD intensities at the Ni  $L_3$ -edge between the full calculations in (a) and the approximations using Eq. 1. The results for different angles  $\varphi_B$  can be found in Fig. S3 of the Supplementary Material.

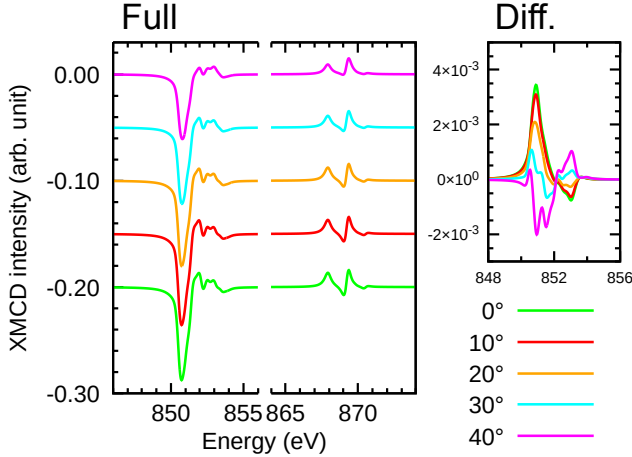


FIG. 6. (a) Ni  $L_{2,3}$ -edge XMCD intensities in  $\text{NiF}_2$  calculated with the magnetic field of 10 T and varying angles  $\varphi_B$ . The light propagation vector  $\hat{\mathbf{k}} = \hat{\mathbf{B}}$  is used in the calculation. (b) The difference of the XMCD intensities between the full calculations in (a) and the approximations of Eq. 2 with  $\alpha = 0.57$  and  $m_0 = 0.12 \mu_B$ .

contribution scales with the amplitude of the magnetization. Moreover, the two contributions exhibit different angular dependencies as the external field rotates away from the easy-axis direction. This distinction provides an opportunity for experimental verification of the peculiar relationship [36] between the x-ray Hall vector and the Néel vector in the rutile structure.

X-ray magneto-optics offers a distinct approach to isolating altermagnetic effects, leveraging the specific influence of valence spin-orbit coupling (SOC) in lighter elements, such as  $3d$  transition metals. The valence SOC modifies the magnetic ground state by inducing canted moments and non-collinearity, while also affecting the excitation energies and the transition matrix elements. These intertwined effects are often difficult to disentangle in transport measurements or visible-range magneto-optics.

In x-ray magneto-optics, however, the dominance of core-level SOC in transition metal elements naturally separates these influences. As a result, the role of valence SOC is largely confined to determining the orientation of magnetic moments, which can also be externally controlled. This separation enables the systematic identification of the valence SOC effects, distinguishing them from the altermagnetic contribution.

#### IV. METHODS

We perform a density functional theory (DFT) calculation for the experimental structure of  $\text{NiF}_2$  [37] using the Wien2K package [38]. The crystal field within the Ni  $3d$  shell is derived from the self-consistent DFT band structure using the Wannier90 and wien2wannier packages [39, 40], see the Supplemental Material for the computational details [34]. Since  $\text{NiF}_2$  is a large-gap Mott insulator, the  $\text{Ni}^{2+}$  atomic model adequately accounts for the Ni  $L_{2,3}$ -edge XAS spectrum dominated by the intra-atomic multiplet effects as shown by the early studies by de Groot *et al.* [20, 41]. The atomic Hamiltonian spanning the space of  $2p$  and  $3d$  shells consisting of the  $3d$

crystal field,  $2p$  and  $3d$  SOC,  $3d-3d$  and  $2p-3d$  Coulomb interaction, Weiss mean-field and the external magnetic field is diagonalized. Full optical conductivity tensor in the Ni  $L_{2,3}$  range is calculated in dipolar approximation using the Fermi golden rule. The total conductivity is the sum of the contributions from the two Ni sublattices in the rutile structure.

The magnetic ground state is obtained with Weiss mean-field theory. The Weiss field acting on local spin (Zeeman field) is calculated with the Heisenberg exchange parameters  $J = 1.47$  meV derived from the experiment [29]. Since the dipole-dipole interaction energy for the studied antiferromagnetic order is degenerate for the all orientations of the Néel vector  $\mathbf{L}$  in the  $ab$ -plane we neglect it in our considerations.

- 
- [1] L. Šmejkal, J. Sinova, and T. Jungwirth, Emerging Research Landscape of Altermagnetism, *Phys. Rev. X* **12**, 040501 (2022).
- [2] L. Šmejkal, J. Sinova, and T. Jungwirth, Beyond Conventional Ferromagnetism and Antiferromagnetism: A Phase with Nonrelativistic Spin and Crystal Rotation Symmetry, *Phys. Rev. X* **12**, 031042 (2022).
- [3] K.-H. Ahn, A. Hariki, K.-W. Lee, and J. Kuneš, Antiferromagnetism in  $\text{RuO}_2$  as  $d$ -wave Pomeranchuk instability, *Phys. Rev. B* **99**, 184432 (2019).
- [4] M. Naka, S. Hayami, H. Kusunose, Y. Yanagi, Y. Motome, and H. Seo, Spin current generation in organic antiferromagnets, *Nature Communications* **10**, 4305 (2019).
- [5] S. Hayami, Y. Yanagi, and H. Kusunose, Momentum-Dependent Spin Splitting by Collinear Antiferromagnetic Ordering, *J. Phys. Soc. Jpn.* **88**, 123702 (2019).
- [6] L. Šmejkal, R. González-Hernández, T. Jungwirth, and J. Sinova, Crystal time-reversal symmetry breaking and spontaneous Hall effect in collinear antiferromagnets, *Sci. Adv.* **6**, eaaz8809 (2020).
- [7] L.-D. Yuan, Z. Wang, J.-W. Luo, E. I. Rashba, and A. Zunger, Giant momentum-dependent spin splitting in centrosymmetric low- $Z$  antiferromagnets, *Phys. Rev. B* **102**, 014422 (2020).
- [8] L.-D. Yuan, Z. Wang, J.-W. Luo, and A. Zunger, Prediction of low- $Z$  collinear and noncollinear antiferromagnetic compounds having momentum-dependent spin splitting even without spin-orbit coupling, *Phys. Rev. Mater.* **5**, 014409 (2021).
- [9] S. Hayami, Y. Yanagi, and H. Kusunose, Bottom-up design of spin-split and reshaped electronic band structures in antiferromagnets without spin-orbit coupling: Procedure on the basis of augmented multipoles, *Phys. Rev. B* **102**, 144441 (2020).
- [10] I. I. Mazin, K. Koepernik, M. D. Johannes, R. González-Hernández, and L. Šmejkal, Prediction of unconventional magnetism in doped  $\text{FeSb}_2$ , *Proc. Natl. Acad. Sci. U.S.A.* **118**, e2108924118 (2021).
- [11] P. Liu, J. Li, J. Han, X. Wan, and Q. Liu, Spin-Group Symmetry in Magnetic Materials with Negligible Spin-Orbit Coupling, *Phys. Rev. X* **12**, 021016 (2022).
- [12] J. Yang, Z.-X. Liu, and C. Fang, Symmetry invariants and classes of quasi-particles in magnetically ordered systems having weak spin-orbit coupling, arXiv:2105.12738.
- [13] L. Šmejkal, A. H. MacDonald, J. Sinova, S. Nakatsuji, and T. Jungwirth, Anomalous Hall antiferromagnets, *Nat. Rev. Mater.* **7**, 482 (2022).
- [14] K. Samanta, M. Ležaić, M. Merte, F. Freimuth, S. Blügel, and Y. Mokrousov, Crystal Hall and crystal magneto-optical effect in thin films of  $\text{SrRuO}_3$ , *J. Appl. Phys.* **127**, 213904 (2020).
- [15] M. Naka, S. Hayami, H. Kusunose, Y. Yanagi, Y. Motome, and H. Seo, Anomalous Hall effect in  $\kappa$ -type organic antiferromagnets, *Phys. Rev. B* **102**, 075112 (2020).
- [16] S. Hayami and H. Kusunose, Essential role of the anisotropic magnetic dipole in the anomalous Hall effect, *Phys. Rev. B* **103**, L180407 (2021).
- [17] R. D. Gonzalez Betancourt, J. Zubáč, R. Gonzalez-Hernandez, K. Geishendorf, Z. Šobáň, G. Springholz, K. Olejník, L. Šmejkal, J. Sinova, T. Jungwirth, S. T. B. Goennenwein, A. Thomas, H. Reichlová, J. Železný, and D. Kriegner, Spontaneous Anomalous Hall Effect Arising from an Unconventional Compensated Magnetic Phase in a Semiconductor, *Phys. Rev. Lett.* **130**, 036702 (2023).
- [18] M. Naka, Y. Motome, and H. Seo, Anomalous Hall effect in antiferromagnetic perovskites, *Phys. Rev. B* **106**, 195149 (2022).
- [19] A. Hariki, Y. Takahashi, and J. Kuneš, X-ray magnetic circular dichroism in  $\text{RuO}_2$ , *Phys. Rev. B* **109**, 094413 (2024).
- [20] A. Hariki, A. Dal Din, O. J. Amin, T. Yamaguchi, A. Badura, D. Kriegner, K. W. Edmonds, R. P. Campion, P. Wadley, D. Backes, L. S. I. Veiga, S. S. Dhesi, G. Springholz, L. Šmejkal, K. Výborný, T. Jungwirth, and J. Kuneš, X-ray Magnetic Circular Dichroism in Altermagnetic  $\alpha$ - $\text{MnTe}$ , *Phys. Rev. Lett.* **132**, 176701 (2024).
- [21] N. Sasabe, M. Mizumaki, T. Uozumi, and Y. Yamasaki, Ferroic Order for Anisotropic Magnetic Dipole Term in Collinear Antiferromagnets of  $(t_{2g})^4$  System, *Phys. Rev. Lett.* **131**, 216501 (2023).
- [22] H. Watanabe, K. Shinohara, T. Nomoto, A. Togo, and R. Arita, Symmetry analysis with spin crystallographic groups: Disentangling effects free of spin-orbit coupling in emergent electromagnetism, *Phys. Rev. B* **109**, 094438

- (2024).
- [23] Z. Feng, X. Zhou, L. Šmejkal, L. Wu, Z. Zhu, H. Guo, R. González-Hernández, X. Wang, H. Yan, P. Qin, X. Zhang, H. Wu, H. Chen, Z. Meng, L. Liu, Z. Xia, J. Sinova, T. Jungwirth, and Z. Liu, An anomalous Hall effect in altermagnetic ruthenium dioxide, *Nat. Electron.* **5**, 735 (2022).
- [24] J. Jiménez-Mier, P. Olalde-Velasco, P. de la Mora, W. Yang, and J. D. Denlinger, Atomic multiplet and charge transfer effects in the resonant inelastic x-ray scattering (rixs) spectra at the nickel  $L_{2,3}$  edge of  $nif_2$ , *Journal of Nuclear Physics, Material Sciences, Radiation and Applications* **5**, 1 (2017).
- [25] J. Kuneš and P. M. Oppeneer, Anisotropic X-ray magnetic linear dichroism at the  $L_{2,3}$  edges of cubic Fe, Co, and Ni: *Ab initio* calculations and model theory, *Phys. Rev. B* **67**, 024431 (2003).
- [26] J. W. Stout and E. Catalano, Thermal anomalies associated with the antiferromagnetic ordering of  $FeF_2$ ,  $cof_2$ , and  $nif_2$ , *Phys. Rev.* **92**, 1575 (1953).
- [27] R. A. Erickson, Neutron Diffraction Studies of Antiferromagnetism in Manganous Fluoride and Some Isomorphous Compounds, *Phys. Rev.* **90**, 779 (1953).
- [28] L. M. Matarrese and J. W. Stout, Magnetic anisotropy of  $NiF_2$ , *Phys. Rev.* **94**, 1792 (1954).
- [29] T. Moriya, Theory of magnetism of  $NiF_2$ , *Phys. Rev.* **117**, 635 (1960).
- [30] N. Stojić, N. Binggeli, and M. Altarelli, Mn  $L_{2,3}$  edge resonant x-ray scattering in manganites: Influence of the magnetic state, *Phys. Rev. B* **72**, 104108 (2005).
- [31] E. Arenholz, G. van der Laan, R. V. Chopdekar, and Y. Suzuki, Anisotropic x-ray magnetic linear dichroism at the  $fe L_{2,3}$  edges in  $fe_3O_4$ , *Phys. Rev. B* **74**, 094407 (2006).
- [32] E. Arenholz, G. van der Laan, R. V. Chopdekar, and Y. Suzuki, Angle-dependent  $ni^{2+}$  x-ray magnetic linear dichroism: Interfacial coupling revisited, *Phys. Rev. Lett.* **98**, 197201 (2007).
- [33] M. W. Haverkort, N. Hollmann, I. P. Krug, and A. Tanaka, Symmetry analysis of magneto-optical effects: The case of x-ray diffraction and x-ray absorption at the transition metal  $L_{2,3}$  edge, *Phys. Rev. B* **82**, 094403 (2010).
- [34] See Supplementary Material for details at ...
- [35] A. S. Borovik-Romanov, A. N. Bazhan, and N. M. Kreines, The weak ferromagnetism of  $NiF_2$ , *Zh. Eksp. Teor. Fiz.* **64**, 1367 (1973).
- [36] A. Hariki, T. Okauchi, Y. Takahashi, and J. Kuneš, Determination of the néel vector in rutile altermagnets through x-ray magnetic circular dichroism: The case of  $MnF_2$ , *Phys. Rev. B* **110**, L100402 (2024).
- [37] J. W. Stout and S. A. Reed, The crystal structure of  $mnf_2$ ,  $fef_2$ ,  $cof_2$ ,  $nif_2$  and  $znf_2$ , *Journal of the American Chemical Society* **76**, 5279 (1954).
- [38] P. Blaha, K. Schwarz, G. Madsen, D. Kvasnicka, and J. Luitz, *WIEN2k, An Augmented Plane Wave + Local Orbitals Program for Calculating Crystal Properties (Karlheinz Schwarz, Techn. Universität Wien, Austria, 2001)*, ISBN 3-9501031-1-2.
- [39] A. A. Mostofi, J. R. Yates, G. Pizzi, Y.-S. Lee, I. Souza, D. Vanderbilt, and N. Marzari, An updated version of wannier90: A tool for obtaining maximally-localised Wannier functions, *Comput. Phys. Commun.* **185**, 2309 (2014).
- [40] J. Kuneš, R. Arita, P. Wissgott, A. Toschi, H. Ikeda, and K. Held, Wien2wannier: From linearized augmented plane waves to maximally localized Wannier functions, *Comput. Phys. Commun.* **181**, 1888 (2010).
- [41] F. M. F. de Groot, J. C. Fuggle, B. T. Thole, and G. A. Sawatzky,  $2p$  X-ray absorption of  $3d$  transition-metal compounds: An atomic multiplet description including the crystal field, *Phys. Rev. B* **42**, 5459 (1990).

## ACKNOWLEDGMENTS

We thank Karel Výborný, Jakub Železný and Anna Kauch for discussions and critical reading of the manuscript. This work was supported by JSPS KAKENHI Grant Numbers 21K13884, 21H01003, 23K03324, 23H03817 (A.H.), and by the project Quantum materials for applications in sustainable technologies (QM4ST), funded as project No. CZ.02.01.01/00/22\_008/0004572 by Programme Johannes Amos Comenius, call Excellent Research and by the Ministry of Education, Youth and Sports of the Czech Republic through the e-INFRA CZ (ID:90254).

# Supplementary Material to “Magnetic Dichroism in Rutile NiF<sub>2</sub>: Separating Altermagnetic and Ferromagnetic Effects”

A. Hariki,<sup>1</sup> K. Sakurai,<sup>1</sup> T. Okauchi,<sup>1</sup> and J. Kuneš<sup>2</sup>

<sup>1</sup>*Department of Physics and Electronics, Graduate School of Engineering, Osaka Metropolitan University, 1-1 Gakuen-cho, Nakaku, Sakai, Osaka 599-8531, Japan*

<sup>2</sup>*Department of Condensed Matter Physics, Faculty of Science, Masaryk University, Kotlářská 2, 611 37 Brno, Czechia*

## I. XMCD SIMULATION

Ni *L*-edge x-ray magnetic circular dichroism (XMCD) spectra were calculated based on the Ni<sup>2+</sup> atomic model. First, density functional theory (DFT) calculations were performed using the WIEN2K package [1] within the local density approximation for the exchange-correlation potential. The experimental rutile structure [2] was employed in the DFT calculations. The crystal-field term,  $h^{\text{CF}}$ , in the atomic model Hamiltonian was derived from the DFT band structure by projecting the Ni *3d* bands near the Fermi level onto a tight-binding model using the wanner90 and wien2wannier packages [3, 4]. The  $h^{\text{CF}}$  term is expressed in the crystal-field basis ( $x'y'$ ,  $3z'^2 - r'^2$ ,  $x'^2 - y'^2$ ,  $z'x'$ ,  $y'z'$ ) with respect to the local coordinate system ( $x'y'z'$ ) shown in Fig. S1 as,

$$h^{\text{CF}} = \begin{pmatrix} -0.107 & 0 & 0 & 0 & 0 \\ 0 & -0.141 & 0.043 & 0 & 0 \\ 0 & 0.043 & -1.058 & 0 & 0 \\ 0 & 0 & 0 & -0.828 & 0 \\ 0 & 0 & 0 & 0 & -0.954 \end{pmatrix}.$$

The core-valence interaction and the *2p* core-orbital spin-orbit coupling (SOC) parameters were estimated using an atomic Hartree-Fock calculation, as described in Refs. [5, 6]. The Slater integrals for the multipole components of the *3d* – *3d* (valence-valence) and *2p* – *3d* (core-valence) interactions in the Ni<sup>2+</sup> atomic model are listed in Table I [7]. The Slater integrals ( $F_2^{dd}$ ,  $F_4^{dd}$ ) for the *3d* – *3d* interaction correspond to a Hund’s exchange parameter  $J = 0.86$  eV, a typical value for Ni<sup>2+</sup> systems. The SOC constants for the Ni *3d* shell,  $\xi = 76$  meV and 83 meV, were obtained from additional DFT calculations for the Ni *3d* model and from the atomic Hartree-Fock calculation, respectively. To account for the hybridization effect with ligands, the SOC value was reduced to  $\xi = 50$  meV, as explained below. The x-ray absorption spectroscopy (XAS) spectral function is expressed using Fermi’s golden rule

$$F_{\text{XAS}}^{(i)}(\omega_{\text{in}}) = -\frac{1}{\pi} \text{Im} \langle g | T^\dagger \frac{1}{\omega_{\text{in}} + E_g - H_i} T | g \rangle.$$

ere,  $|g\rangle$  represents the ground state with energy  $E_g$ , and  $\omega_{\text{in}}$  denotes the energy of the incident photon. The operator  $T$  corresponds to the electric dipole transition operator for circularly-polarized x-rays. The index  $i$  ( $i = 1, 2$ ) identifies

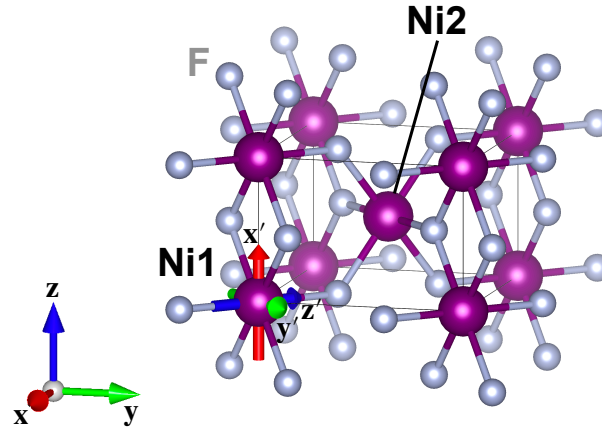


FIG. S1. The crystal structure of NiF<sub>2</sub> and a local coordinate ( $x'y'z'$ ).

the x-ray excited Ni site within the unit cell. The atomic Hamiltonian  $H_i$  for each Ni site is used to calculate its individual contribution to the spectra [8, 9]. The total XMCD intensities are then obtained by summing the contributions from the two sites.

	$F_2^{dd}$	$F_4^{dd}$	$F_2^{pd}$	$G_1^{pd}$	$G_3^{pd}$
Values (eV)	7.409	4.631	6.563	4.919	2.797

TABLE I. The atomic Slater integral values for the  $3d - 3d$  (valence-valence) and  $2p - 3d$  (core-valence) interaction employed in the  $\text{Ni}^{2+}$  atomic model. Here,  $F$  and  $G$  denote the direct and exchange integrals, respectively.

## II. $\text{NiF}_6$ CLUSTER MODEL SIMULATION

In Fig. S4, we compare the energy splittings within the lowest  $S = 1$  states between the  $\text{NiF}_6$  cluster model and the  $\text{Ni}^{2+}$  atomic model. The hybridization parameters in the  $\text{NiF}_6$  cluster model, summarized in Table II, were derived from the tight-binding model Hamiltonian, which explicitly represents both the Ni  $3d$  and F  $2p$  DFT bands (see Ref. [10] for the construction method of the cluster model). The averaged Coulomb interaction  $U_{dd}$  and the charge-transfer energy  $\Delta_{CT}$  values were adopted from Ref. [11]. The cluster model incorporates  $\xi = 83$  meV, obtained from the atomic Hartree-Fock calculation. The atomic model with  $\xi = 50$  meV reproduces a similar splitting,  $\Delta_1$ , between the lowest and the first excited states as that obtained in the  $\text{NiF}_6$  cluster model. Thus, we use the reduced value  $\xi = 50$  meV in our atomic model calculations to incorporate hybridization effect with ligands. The atomic model with  $\xi = 50$  meV yields a ferromagnetic canting moment of about  $0.03 \mu_B$ , as shown in Fig. 4(c) in the main text, consistent with estimate in previous studies [12, 13].

	$U_{dd}$	$\Delta_{CT}$	$V_{B_{1g}}$	$V_{A_g}$	$V_{A'_g}$	$V_{B_{2g}}$	$V_{B_{3g}}$
Values (eV)	6.50	4.30	2.18	2.06	1.19	1.06	1.18

TABLE II. The parameter values for configuration-averaged  $3d - 3d$  Coulomb interaction ( $U_{dd}$ ), charge-transfer energy ( $\Delta_{CT}$ ) and the metal-ligand hybridization amplitude adopted in the  $\text{NiF}_6$  cluster model in eV unit.  $U_{dd}$  and  $\Delta_{CT}$  are taken from Ref. [11].

		$\text{NiF}_6$ cluster ( $\xi=0.083\text{eV}$ )	Atomic model ( $\xi=0.083\text{eV}$ )	Atomic model ( $\xi=0.050\text{eV}$ )
$ \text{Ex}2\rangle$	$\Delta_2$			
$ \text{Ex}1\rangle$	$\Delta_1$	$\Delta_1$ (meV)	0.52	1.08
$ \text{GS}\rangle$		$\Delta_2$ (meV)	0.66	0.67

FIG. S2. The energy splittings between the ground state and the first excited state ( $\Delta_1$ ), as well as between the first and second excited states ( $\Delta_2$ ) within the lowest  $S = 1$  states, are shown for the  $\text{NiF}_6$  cluster model and the atomic model in meV unit. For the atomic model, simulations were conducted with two different SOC constants  $\xi$ .

- [1] P. Blaha, K. Schwarz, G. Madsen, D. Kvasnicka, and J. Luitz, *WIEN2k, An Augmented Plane Wave + Local Orbitals Program for Calculating Crystal Properties* (Karlheinz Schwarz, Techn. Universitat Wien, Austria, 2001), ISBN 3-9501031-1-2.
- [2] J. W. Stout and S. A. Reed, *Journal of the American Chemical Society* **76**, 5279 (1954).



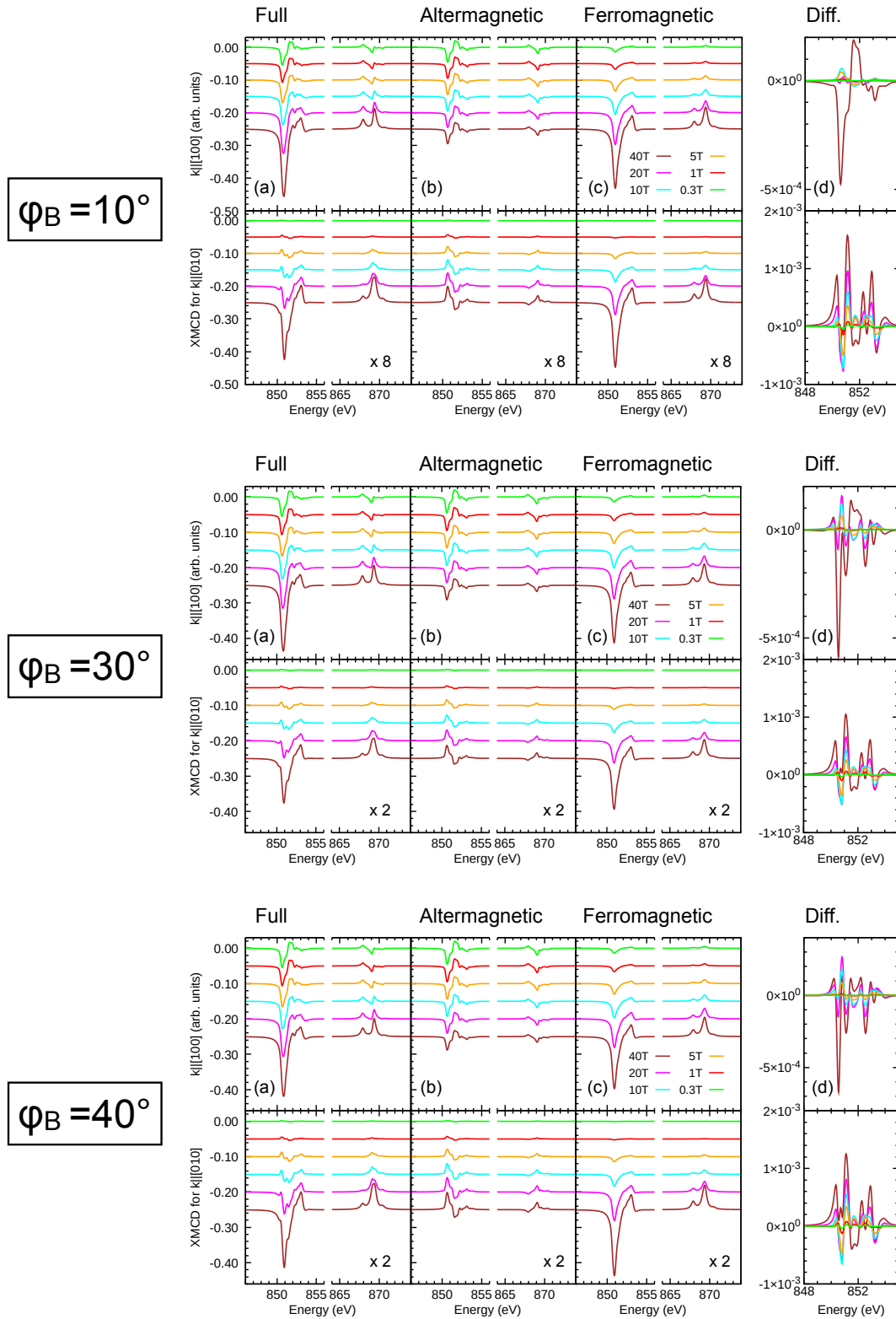


FIG. S3. (a) Ni  $L_{2,3}$ -edge XMCD intensities in  $\text{NiF}_2$  calculated for various amplitudes of the magnetic field  $B$  with  $\varphi_B = 10^\circ$  (top),  $30^\circ$  (middle), and  $40^\circ$  (bottom) for the two geometries of the light propagation vector  $\hat{\mathbf{k}} = [\text{100}]$  (top) and  $\hat{\mathbf{k}} = [\text{010}]$  (bottom). (b) The altermagnetic contributions and (c) the ferromagnetic contributions. (d) The difference in the XMCD intensities at the Ni  $L_3$ -edge between the full calculations in (a) and the approximations using Eq. 1 in the main text.

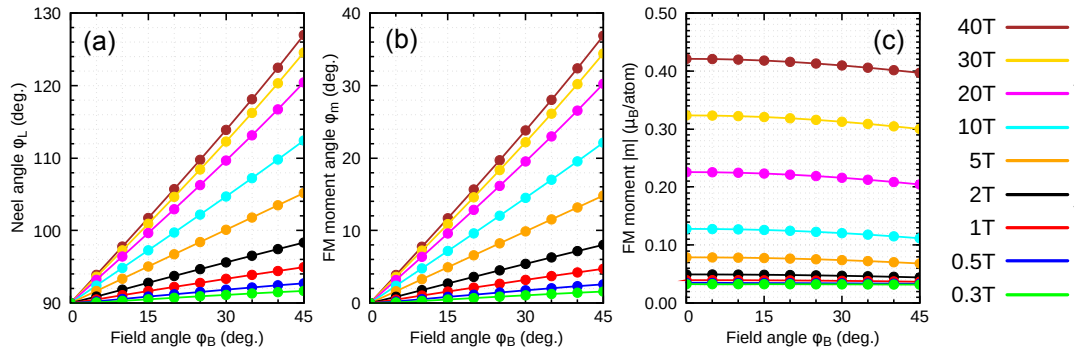


FIG. S4. Relation between the angles of the external field  $\varphi_B$  and (a) the Néel vector  $\varphi_L$ , (b) the FM moment  $\varphi_m$ , and (c) the amplitude of the FM moment  $|m(\mathbf{B})|$  for selected amplitudes of the external field  $\mathbf{B}$ .

- [3] A. A. Mostofi, J. R. Yates, G. Pizzi, Y.-S. Lee, I. Souza, D. Vanderbilt, and N. Marzari, *Comput. Phys. Commun.* **185**, 2309 (2014).
- [4] J. Kuneš, R. Arita, P. Wissgott, A. Toschi, H. Ikeda, and K. Held, *Comput. Phys. Commun.* **181**, 1888 (2010).
- [5] A. Hariki, T. Uozumi, and J. Kuneš, *Phys. Rev. B* **96**, 045111 (2017).
- [6] A. Hariki, M. Winder, T. Uozumi, and J. Kuneš, *Phys. Rev. B* **101**, 115130 (2020).
- [7] In the atomic model, the monopole terms  $F_0^{dd}$  and  $F_0^{pd}$  only contribute to an overall energy shift and are therefore not relevant to our analysis.
- [8] A. Hariki, Y. Takahashi, and J. Kuneš, *Phys. Rev. B* **109**, 094413 (2024).
- [9] M. Winder, A. Hariki, and J. Kuneš, *Phys. Rev. B* **102**, 085155 (2020).
- [10] T. Yamaguchi, K. Higashi, A. Regoutz, Y. Takahashi, M. Lazemi, Q. Che, F. M. F. de Groot, and A. Hariki, *Phys. Rev. B* **109**, 205143 (2024).
- [11] K. Okada and A. Kotani, *J. Phys. Soc. Japan* **60**, 772 (1991).
- [12] L. M. Matarrese and J. W. Stout, *Phys. Rev.* **94**, 1792 (1954).
- [13] T. Moriya, *Phys. Rev.* **117**, 635 (1960).